

Propagating surfaces in isotropic turbulence

By S. S. GIRIMAJI¹ AND S. B. POPE²

¹A. S. & M. Inc., Hampton, VA 23666, USA

²Sibley School of Mechanical and Aerospace Engineering, Cornell University,
Ithaca, NY 14853, USA

(Received 2 October 1990 and in revised form 17 June 1991)

Propagating surface evolution in isotropic turbulence is studied using velocity fields generated by direct numerical simulations. The statistics of tangential strain rate, fluid velocity, characteristic curvature and area-following propagating surface elements are investigated. The one-time statistics of strain rate and fluid velocity pass monotonically from Lagrangian value at low propagation speeds to Eulerian values at high speeds. The strain-rate statistics start deviating significantly from the Lagrangian values only for propagating velocities greater than the Kolmogorov velocity scale v_η , whereas, with fluid-velocity statistics the deviation occurs only for velocities greater than the turbulence intensity u' . The average strain rate experienced by a propagating surface decreases from a positive value to near zero with increasing propagation velocity. The autocorrelation function and frequency spectrum of fluid velocity and strain rate scale as expected in the limits of small and large propagation velocities. It is also found that for the range of propagation velocities considered, an initially plane surface element in turbulence develops a cusp in finite time with probability nearly one. The evolution of curvature is studied using the concept of *hitting time*. Initially plane propagating surfaces end up being almost cylindrical in shape. Highly curved surface elements are associated with negative strain rates and small surface areas.

1. Introduction

A propagating surface in fluid flow is defined as a surface that propagates normal to itself relative to the fluid. Propagating surfaces are of practical value in the study of premixed combustion. A complete solution to the turbulent premixed combustion problem requires that the coupled chemical-kinetics and turbulence equations be solved simultaneously. If the timescale of the thermochemistry is smaller than any timescale of the turbulence and if the chemical kinetics are independent of the strain rate experienced by the flame, the burning is restricted to thin sheets called flamelets. A flamelet by definition is thin compared to any lengthscale in turbulence and this regime of premixed combustion is called the flamelet regime. In the flamelet regime of premixed combustion the turbulence manifests itself on the combustion only via its effect on the propagating flamelet. The flamelet propagates into the reactants, leaving behind burnt products of lower density and higher temperature. The propagating velocity of the flamelet in turbulent combustion is a function of the local strain rate and curvature of the flamelet. It is clear that a good understanding of the behaviour of propagating flamelets is important for the accurate modelling of turbulent combustion in this regime.

As a first step towards understanding the behaviour of propagating flamelets, in

this work we study passive, infinitesimally thin, regular surfaces (with no inner holes) propagating at constant velocity in a constant-density turbulence field. Thus the simplifications effected to the flamelet are: (i) the surface propagation speed is constant at the characteristic laminar flame speed of the mixture; and (ii) the density jump across the flamelet is zero. (Peters 1988, refers to flame surfaces propagating at constant velocity as flame sheets.) The effect of turbulence on such a passive surface is to convect, stretch and bend it. These random processes are important from the combustion viewpoint and the objective of this work is to characterize their statistics. Of particular interest is the question of whether the curvature of an initially plane surface becomes infinite (i.e. if the surface develops a singularity or cusp) in finite time.

Global description of a finite-sized propagating surface is rendered difficult by the diffusive nature of turbulence. A local one-point description of the surface properties is a good starting point (Pope 1988) and is the subject of the present study. Although this one-point study cannot answer important questions that involve the global description of the flamelet, it will provide valuable insight into the local geometry of its structure. Other types of surfaces of interest, material and constant property, can also be viewed as propagating surfaces. The material surface propagates with zero velocity and the position-dependent propagation velocity of the constant-property surface is a known function of the Eulerian scalar field in question (Pope 1988).

1.1. *A brief literature review*

Of all types of surfaces, material surfaces have received most attention in the literature. Analytical works in this area include those of Batchelor (1952, 1959) and Kraichnan (1974). Recently Yeung, Girimaji & Pope (1990), Pope, Yeung & Girimaji (1989), Girimaji & Pope (1990), and Girimaji (1991) have used velocity fields generated by direct numerical simulations (DNS) to study the effect of isotropic turbulence on material line, area and volume elements. Drummond & Münch (1990, 1991) have also studied material element deformation and distortion numerically, but using a simple random flow field.

The studies of propagating surfaces in the literature are more recent. Using the data of material elements Yeung *et al.* (1990) infer the behaviour of surface elements propagating at velocities much smaller than the Kolmogorov velocity scale. They show that these surfaces are trapped close to material surfaces with which they are initially coincident. Consequently the behaviour of slowly propagating surfaces is deduced to be similar to that of material surfaces. Pope (1988) has derived the evolution equations for the surface-normal, area and curvature-following infinitesimal propagating surfaces in terms of velocity derivatives following the elements. Flame-front propagating in simple flow fields has been studied by Ashurst, Shivashinsky & Yakhot (1988). They suggest that for sufficiently small propagating velocities there is no cusp formation.

1.1.1. *Analogy with inertial particles*

The evolution of passive propagating elements in turbulence is somewhat analogous to that of particles with inertia at small particle loading densities. Elements of vanishingly small propagation velocity and inertia behave like fluid particles; hence, the velocity field statistics of these elements are close to the Lagrangian statistics. At the other limit, elements of infinite propagation velocity or inertia experience a turbulence field that appears frozen in time; hence, the one-time velocity field statistics following these elements are nearly identical to the

corresponding Eulerian statistics. The main difference is that in the present case the magnitude of the relative velocity between the propagating and the fluid particles is constant whereas in the case of inertial particles the relative velocity is governed by a differential equation. The evolution of inertial particles in turbulence has received a good deal of attention in the literature (e.g. Csanady 1970) and some of the ideas developed in that context are used in the present study. In particular the *crossing trajectories effect* concept is used to explain some of the observed behaviour of the propagating elements.

Crossing trajectories effect. Consider a propagating element E in a turbulence structure of lengthscale λ and timescale τ . At time $T = 0$, let this propagating element be coincident with a fluid element F . Let the element E propagate with respect to the fluid at a constant velocity P . Owing to the relative motion, the element E continuously changes its fluid particle neighbourhood. The timescale τ_E of the change of fluid velocity following the element E is

$$\tau_E \sim \min \left\{ \frac{\lambda}{P}, \tau \right\}, \quad (1)$$

whereas the timescale of change following the fluid element F is τ .

For low propagation velocities ($P \ll \lambda/\tau$) the timescales of the elements E and F are nearly equal and their trajectories deviate little with time. However at large propagation velocities ($P > \lambda/\tau$) the element E cuts through (or falls out of) the eddy losing its memory faster than the fluid element F which changes its velocity owing to eddy decay alone. Hence the crossing trajectories effect increases with propagation velocity: slowly propagating elements experiencing longer timescales of correlation than rapidly propagating elements. By the same token, for any given propagation velocity the crossing trajectories effect is negligible if the lengthscale is large enough ($\lambda \gg P\tau$) and is important otherwise, especially for $\lambda < P\tau$.

Having motivated the study of passively propagating surfaces in turbulence and briefly reviewed the related literature we now present study.

1.2. Definitions

To facilitate further discussion we now define various quantities of interest. We consider an incompressible, statistically stationary, isotropic turbulence field of Taylor-scale Reynolds number R_λ , turbulence intensity U' and the integral timescale T_U . The small scales are characterized by τ_η , η and v_η – the Kolmogorov time, length and velocity scales respectively. We expect the small-scale processes and the velocity gradient statistics to scale with the Kolmogorov scales. For this reason, throughout the remainder of the paper all the quantities considered are normalized with the Kolmogorov scales. However it is expected that the (Kolmogorov-normalized) fluid-velocity statistics scale with the (normalized) turbulence intensity $u' (\equiv U'/v_\eta)$ and with the (normalized) integral timescale $T_u (\equiv T_U/\tau_\eta)$.

Evolving in this isotropic turbulent field is an infinitesimal surface element propagating normal to itself at a constant (normalized) velocity p relative to the fluid. At any time t , $\mathbf{N}(t)$ is the surface-normal vector. Following Pope (1988), we describe the evolution of the surface in a Cartesian coordinate system that moves with the surface element. By convention the 3-axis is taken to be surface-normal direction. The 1- and 2-axes are situated on the tangent plane of the surface and rotate with the fluid about the 3-axis. The unit vectors of the Cartesian coordinate system, \mathbf{e}_1 , \mathbf{e}_2 and \mathbf{e}_3 , evolve according to the equations given in §1.3. The fluid

velocity following the propagating element is denoted by $U(t)$. The strain-rate tensor \mathbf{s} is defined as

$$s_{ij} = \frac{1}{2}[U_{i,j} + U_{j,i}], \quad i, j = 1, 2, 3. \quad (2)$$

$U_{i,j}$ denotes the derivative of the i th component of velocity in the j th direction. The tangential strain rate, denoted by a , is

$$a = U_{1,1} + U_{2,2} = -U_{3,3}, \quad (3)$$

the last equality being a consequence of incompressibility. The second derivative of U_3 in the tangential plane of the surface is a second-order tensor denoted by $U_{3,\alpha\beta}$. Here and throughout the rest of the paper Greek subscripts indicate components of tensors along the tangential plane and hence are restricted values 1 or 2.

At time t , $S(t)$ is the infinitesimal area of the element, $A(t) (\equiv S(t)/S(0))$ is the area ratio, and, \mathbf{h} is the symmetric two-dimensional second-order curvature tensor of the propagating surface (Pope 1988). The eigenvalues of \mathbf{h} (k_1 and k_2) are called the principal curvatures of the surface elements. By convention we take $|k_1| \geq |k_2|$. Clearly the eigenvalues and hence k_1 and k_2 can be positive or negative. Propagation tends to decrease the radius of curvature when the curvature of a surface is positive. Conversely, propagation tends to flatten out a surface of negative curvature. The characteristic curvature C is defined as,

$$C \equiv (k_1^2 + k_2^2)^{\frac{1}{2}} = (h_{\alpha\beta}h_{\alpha\beta})^{\frac{1}{2}}. \quad (4)$$

The characteristic radius of curvature R of the surface element is defined as

$$R \equiv 1/C. \quad (5)$$

In thus defining the characteristic curvature and characteristic radius of curvature the information about the sign of curvature is lost. Given C alone one cannot answer the question of whether propagation will increase or decrease the value of the characteristic curvature. To answer that question further information about the surface element orientation is required. The second-order tensor $g_{\alpha\beta}$ defined as,

$$g_{\alpha\beta} = h_{\alpha\beta}/C, \quad (6)$$

clearly contains that information. (Note that $g_{\alpha\beta}g_{\alpha\beta} = 1$.)

1.3. Evolution equations

The position vector $X(t)$ of a propagating element evolves according to

$$\frac{dX(t)}{dt} = U(X(t)) + pN. \quad (7)$$

Pope (1988) has derived evolution equations for the normal $N(t)$ area ratio $A(t)$, and curvature $\mathbf{h}(t)$, following propagating elements in the time-dependent Cartesian coordinate system described in the previous subsection. Given the initial surface orientation, the normal $N(\equiv \mathbf{e}_3)$ evolves according to

$$\frac{d\mathbf{e}_3}{dt} = -\mathbf{e}_\alpha U_{3,\alpha}. \quad (8)$$

The tangential-plane unit vectors \mathbf{e}_1 and \mathbf{e}_2 evolve according to

$$\frac{d\mathbf{e}_\alpha}{dt} = \frac{1}{2}(U_{\beta,\alpha} - U_{\alpha,\beta})\mathbf{e}_\beta + U_{3,\alpha}\mathbf{e}_3. \quad (9)$$

The curvature tensor evolves according to

$$\frac{dh_{\alpha\beta}}{dt} = U_{3,\alpha\beta} - ah_{\alpha\beta} - (s_{\gamma\beta}h_{\alpha\gamma} + s_{\gamma\alpha}h_{\beta\gamma}) + ph_{\alpha\gamma}h_{\gamma\beta}. \quad (10)$$

The area ratio following the propagating surface evolves according to

$$\frac{d \ln A}{dt} = a - p(k_1 + k_2) = a - ph_{\alpha\alpha}. \quad (11)$$

The second term in (11) represents the stretching of the surface area due to straining by the flow field. The third term represents the fractional rate of change of area due to propagation.

The equation for the characteristic curvature can be derived from (10):

$$\frac{dC}{dt} = b_1 + b_2 C + b_3 C^2, \quad (12)$$

where the bending term b_1 is

$$b_1 = U_{3,\alpha\beta}g_{\alpha\beta},$$

the stretching coefficient b_2 is

$$b_2 = -a - 2s_{\alpha\beta}g_{\beta\gamma}g_{\gamma\alpha},$$

and the propagation coefficient b_3 is

$$b_3 = pg_{\alpha\beta}g_{\beta\gamma}g_{\gamma\alpha}.$$

Note that b_1 , b_2 and b_3 are functions of a statistically stationary Eulerian velocity field and a tensor of unit norm and hence can be expected to be stationary random variables. The bending term initiates curvature on an initially plane surface. Then the effects of straining and propagation takeover, perhaps causing the curvature to become infinite in finite time. That the propagation term can cause a cylindrical surface with some non-zero initial curvature to develop a singularity (i.e. zero radius or infinite curvature, also called a cusp) can be seen from the following simplified equation for the radius of curvature. Consider the case when $k_1 > 0$ and $k_2/k_1 \approx 0$ so that $R \approx 1/k_1$. In the absence of bending and straining the evolution equation of R can be derived from (12) to be

$$\frac{dR}{dt} = -p. \quad (13)$$

The solution for (13) is

$$R(t) = R_0 - pt. \quad (14)$$

So under the influence of propagation alone, a surface of non-zero initial radius (R_0) attains singularity at time $t = R_0/p$. Whether a turbulence flow field (where bending and stretching are also present) can cause an initially plane surface to develop singularity in finite time is not clear and is one of the questions addressed in this paper.

1.4. Specific objectives of the present study

Numerically generated turbulence is used to study the following aspects of propagating-surface evolution as a function of the propagating velocity:

- (i) the one-time statistics, autocorrelation and frequency spectrum of the fluid velocity normal to the surface ($U_3(t)$) following a propagating element;
- (ii) the one-time statistics, autocorrelation and frequency spectrum of the tangential strain rate ($a(t)$) following a propagating element;
- (iii) the correlation between normal fluid velocity ($U_3(t)$) and tangential strain rate ($a(t)$) of a propagating element;
- (iv) the evolution of the characteristic curvature $C(t)$ and surface area ratio $A(t)$ of the propagating element.

The remainder of the paper is organized as follows. In §2 the numerical methods employed are discussed. In §3 the statistics of velocity and strain rate are presented. The evolution of curvature is investigated in §4. Section 5 summarizes our conclusions.

2. Numerical methods

In this Section the numerical methods employed in this study are briefly discussed. In §2.1, the DNS technique used to generate velocity-field time series following the propagating elements are described. In §2.2, we describe the procedure for obtaining surface properties from the velocity-field time series.

2.1. Direct numerical simulations

The direct numerical simulations performed for this paper are similar to those of Pope *et al.* (1989), using the same parameters but a different initial field, resulting in a different realization of the turbulence. For completeness some important details of the simulations are provided below.

A modified version of Rogallo's (1981) pseudo-spectral code is used to solve the Navier–Stokes equations in a cubical box (of 64^3 grid nodes) with periodic boundary conditions. Without affecting the dynamics of the high wavenumbers, energy is added to the low wavenumbers to maintain the turbulence stationary (Eswaran & Pope 1988; Yeung & Pope 1989). The kinematic viscosity is chosen to yield a spatial resolution adequate for resolving velocity second derivatives (Pope *et al.* 1989). Such a choice of viscosity yields a Taylor-scale Reynolds number (R_λ) of 37. The Kolmogorov length, time and velocity scales for this simulation are 0.0486, 0.0961 and 0.506 respectively. The turbulence intensity ($u' = U'/v_\eta$) is 3.20. Further details about the parameters of the simulation are given in Pope *et al.* (1989).

For material surfaces a constant time-step of $\Delta t_m = 0.052\tau_\eta$ was found to be adequate (Pope *et al.* 1989). This time-step yielded a Courant number of approximately $\frac{1}{2}$ for the largest fluid velocity encountered over the entire simulation. The time-step used for the propagating surface is

$$\Delta t_p = \Delta t_m \frac{u'}{u' + p}, \quad (15)$$

which corresponds to a Courant number of approximately $\frac{1}{2}$ for the largest total (propagating + fluid) velocity encountered over the entire simulation.

Starting from a specified initial spectrum the turbulence is allowed to evolve until the Eulerian field becomes statistically stationary. Then at time $t = 0$, a total of $I = 8192$ randomly placed and oriented fluid elements are released. The particle position evolution equation, (7), is integrated using a second-order Runge–Kutta scheme. The velocity and its first derivative at the particle locations are calculated from the corresponding Eulerian fields using the cubic-spline interpolation algorithm of Yeung & Pope (1988). The second derivative of velocity is obtained by differentiating the velocity-derivative spline.

Eight simulations with identical initial conditions and turbulence parameters are performed for propagation velocities ranging from $0.25v_\eta$ to $32v_\eta$. The total number of time-steps for each propagating velocity is 1500. The total length of the time series for a propagating velocity p is

$$t_{fp} = \frac{78u'}{u' + p}, \quad (16)$$

approximately $70\tau_\eta$ for the lowest propagating velocity and $7\tau_\eta$ for the highest. So, although the realization of the turbulence is the same for all the propagation velocities, the total length of the time record decreases with increasing p . For all propagation velocities, the total distance traversed by a typical propagating particle over the period of simulation corresponds to approximately twice the length of the computational box. Hence the duration of the simulations is adequate.

2.2. Calculation of surface properties

At time $t = 0$, given the normal vector (\mathbf{e}_3), the direction of the unit vector \mathbf{e}_1 can be chosen at random on the tangent plane, and \mathbf{e}_2 specified to complete a right-handed-Cartesian coordinate system. For convenience these directions are made initially coincident with the computational axes. Since the turbulence field is isotropic, this initial condition represents random orientation of the propagating surface elements with respect to the velocity field. The initial values of area ratio and curvature are unity and zero respectively. Knowing the velocity first and second derivatives, the surface curvature equations (8)–(11) are integrated from the aforementioned initial conditions to yield the surface properties at subsequent times.

The equations for the unit vectors of the Cartesian coordinate system $\mathbf{e}_i(t)$, and the area ratio $A(t)$, are all solved using second-order Runge–Kutta schemes. The equation for the components of the curvature $h_{\alpha\beta}$ poses a problem, for the curvature of a propagating surface is found to become infinite in finite time. Conventional numerical procedures are likely to yield solutions fraught with truncation errors at large but finite curvatures. Motivated by the exact solution at high curvatures to the radius of curvature equation, (13), a predictor–corrector scheme that integrates the $h_{\alpha\beta}$ equation accurately at high curvatures is devised. The full curvature equation, (10), can be restated as

$$\frac{d\mathbf{h}}{dt} = \mathbf{G} + p\mathbf{h} \cdot \mathbf{h}, \tag{17}$$

where
$$G_{\alpha\beta} = U_{3,\alpha\beta} - ah_{\alpha\beta} - (s_{\gamma\beta}h_{\alpha\gamma} + s_{\gamma\alpha}h_{\beta\gamma}). \tag{18}$$

Then the predictor \mathbf{h}' at time t is given by

$$\mathbf{h}'(t) = (\mathbf{I} - \mathbf{h}(t)p\Delta t)^{-1}(\mathbf{h}(t) + \mathbf{G}(\mathbf{h}, t)\Delta t). \tag{19}$$

The corrector step that yields the value of \mathbf{h} at time $t + \Delta t$ is

$$\mathbf{h}(t + \Delta t) = (\mathbf{I} - \mathbf{h}(t)p\Delta t)^{-1}[\mathbf{h}(t) + \frac{1}{2}\Delta t\{\mathbf{G}(\mathbf{h}) + \mathbf{G}(\mathbf{h}')\} + \mathbf{H}]. \tag{20}$$

In the above equation,

$$H_{\alpha\beta} = \frac{1}{2}p\Delta t(h'_{\alpha\beta}h_{\gamma\beta} - h_{\alpha\gamma}h'_{\gamma\beta}). \tag{21}$$

The \mathbf{H} -term in the corrector step is required to make the scheme second-order accurate.

As mentioned earlier, the initial value of curvature is zero for all elements. With passage of time the value of curvature increases and for most elements becomes infinite before the end of the computations. At each step, each surface element is tested for cusp formation. At time t , surface-element curvatures which are such that

$$h_{\alpha\beta} > 1/p\Delta t \tag{22}$$

are identified. Under the influence of the propagation term, the characteristic curvature (calculated according to (19), (20)) of these elements may become zero and pass on to negative values over the next time-step.† The zero value represents cusp

† It is possible though that the bending and stretching terms prevent the characteristic curvature from going to zero. But at these high values of curvatures the propagation term is the leading-order term and hence can be expected to dominate the curvature evolution.

formation after which the curvature equation, (10), is invalid. In the calculations, the elements whose curvature are large enough to satisfy (22) are deemed to have attained singularity and the calculation of their curvature h and area ratio A is discontinued. The particle tracking, interpolation and calculation of the surface normal continue since these quantities do not involve curvature. The maximum value of curvature – that is distinct from infinity – permitted by the criterion expressed in (22) is

$$C_{\max}(p) = 2/p\Delta t. \quad (23)$$

3. Strain rate and fluid velocity

Consider an ensemble of initially randomly located and oriented surface elements, propagating through stationary isotropic turbulence. The fluid velocity and its gradients following the elements are random processes. After an initial transient period of a few Kolmogorov timescales (for surface reorientation is a small-scale phenomenon) these random processes attain stationary distributions that are independent of the initial conditions of the elements. In this Section, the one-time statistics, autocorrelation, and spectrum of the strain rate and fluid velocity following propagating elements at this stationary state are discussed. The cross-correlation between strain rate and velocity is also presented.

3.1. Strain-rate statistics

It was seen in Girimaji & Pope (1990) that strain rates following fluid elements are somewhat persistent. This causes the surface normal (e_3) to preferentially orientate along the maximum negative strain-rate direction. As a result the mean tangential strain rate ($\langle a \rangle$) is positive. The strain rates experienced by propagating elements are, however, less persistent due to crossing trajectories effect. With increasing propagation velocities the elements cut through eddies more and more rapidly, causing the strain rates to be less and less persistent. So the proclivity of the surface normal to point along the maximum strain-rate direction decreases and with it the magnitude of $\langle a \rangle$ diminishes.

The stationary values of the mean and variance of the tangential strain rate a (recall that all the quantities are normalized by Kolmogorov scales) are plotted against propagation velocity in figure 1. For small propagation velocities these statistics are very close to the values for material surfaces given in Girimaji & Pope (1990). (The Lagrangian values are $\langle a \rangle = 0.160$ and $\text{var}(a) = 0.09$.) At large propagation velocities the mean and variance approach the Eulerian values of 0 and 0.05 respectively. The transition from the Eulerian to the Lagrangian values appears monotonic. For propagating velocities smaller than v_η ($p < 1$) the deviations from the Lagrangian values are negligible. This is because at these propagation velocities the crossing trajectories effect is negligible.

3.1.1. Autocorrelation of strain rate

The autocorrelation function $f_a(t')$ and the correlation time-scale Θ_a of the strain-rate process are defined as

$$f_a(t') = \frac{1}{\text{var}(a)} \langle [a(t) - \langle a \rangle][a(t+t') - \langle a \rangle] \rangle, \quad (24)$$

and

$$\Theta_a = \int_0^\infty |f_a(t')| dt'. \quad (25)$$

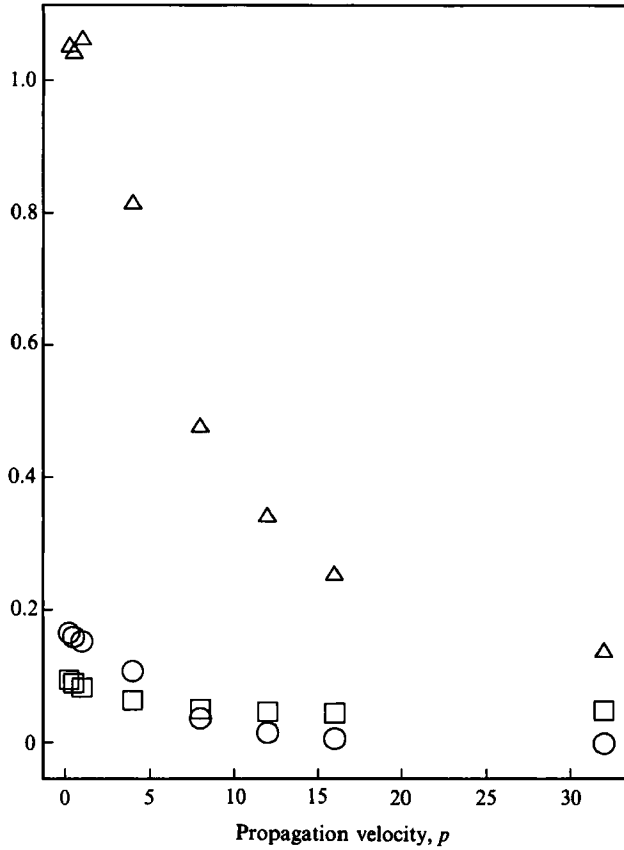


FIGURE 1. Strain-rate statistics vs. propagation velocity: $\langle a \rangle$ (○), $\text{var}(a)$ (□), θ_a (△).

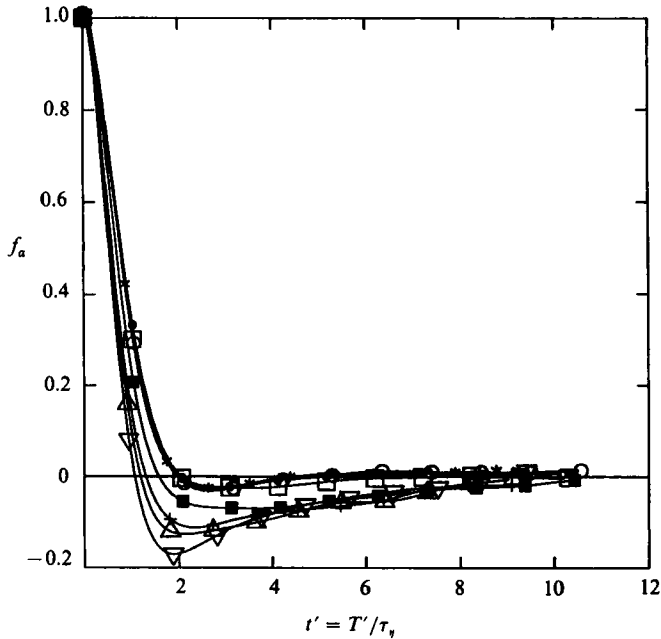


FIGURE 2. Autocorrelations of strain rate in scaled time: $p = \frac{1}{2}$ (○), $p = \frac{1}{2}$ (●), $p = 1$ (*), $p = 4$ (□), $p = 8$ (■), $p = 12$ (+), $p = 16$ (△), $p = 32$ (▽).

If there is a negative loop in the correlation function, the timescale thus defined is a better indicator of the time over which the strain rate is correlated with itself – rather than the usual definition ($\Theta_a = \int_0^\infty f_a(t') dt'$).

The behaviour of $f_a(t')$ and Θ_a at large propagating velocities can be analysed as follows. At large propagation velocities the strain rate and bending experienced by the element become less and less persistent. As p tends to infinity the integral of the right hand-side of (8) over any finite time tends to zero, resulting in

$$\mathbf{e}_3(t) = \mathbf{e}_3(0). \quad (26)$$

Since the initial orientation of the surface normal is arbitrary and the turbulence is isotropic, $\mathbf{e}_3(0)$ can be made to coincide with an Eulerian, Cartesian coordinate axis, say the 3-axis. Since the propagation velocity along $\mathbf{e}_3(t)$ ($\approx \mathbf{e}_3(0)$) is much larger than the fluid velocity, the particle propagates through the turbulence field in a straight line along the 3-axis. So.

$$\frac{dX_3}{dt} \approx p, \quad (27)$$

leading to

$$\langle [a(t) - \langle a \rangle][a(t+t') - \langle a \rangle] \rangle = \langle [a(X_3(t), t) - \langle a \rangle][a(X_3(t) + pt', t+t') - \langle a \rangle] \rangle. \quad (28)$$

If p tends to infinity and t' tends to zero maintaining pt' finite, the following approximation is valid:

$$\begin{aligned} f_a(t') &= \frac{1}{\text{var}(a)} \langle [a(X_3(t), t) - \langle a \rangle][a(X_3(t) + pt', t+t') - \langle a \rangle] \rangle \\ &\approx \frac{1}{\text{var}(a)} \langle [a(X_3(t), t) - \langle a \rangle][a(X_3(t) + pt', t) - \langle a \rangle] \rangle \\ &= F_a(pt'), \end{aligned} \quad (29)$$

where, F_a is the one-dimensional Eulerian space-correlation function of the velocity gradient $\partial U_3/\partial x_3$ (recall $a = -\partial U_3/\partial x_3$). Since in isotropic turbulence U_3 is homogeneous in space, the spatial autocorrelation of $\partial U_3/\partial x_3$ is such that

$$\int_0^\infty F_a(x'_3) dx'_3 = 0. \quad (30)$$

Using (29) and (25), the correlation timescale for large propagation velocities can be written as

$$\Theta_a = \frac{1}{p} \int_0^\infty |F_a(pt')| d(pt') = \frac{1}{p} \mathcal{A}_a, \quad (31)$$

where \mathcal{A}_a is the correlation lengthscale of $\partial U_3/\partial x_3$ in isotropic turbulence.

The variation of Θ_a with p is plotted in figure 1. As with the one-time statistics the deviation from Lagrangian values is small for small propagation velocities. The log-log version of figure 1 (not shown) indicates that at the high- p end, Θ_a decreases as p^{-1} as suggested by (31).

The autocorrelation function $f_a(t')$ in scaled time t'/Θ_a is presented in figure 2 for various propagating velocities. It is mostly positive for slowly propagating velocities, as in the case of material surface, Yeung *et al.* (1990). At high propagation velocities the function develops a negative loop which is characteristic of the Eulerian velocity-gradient correlation in (29).

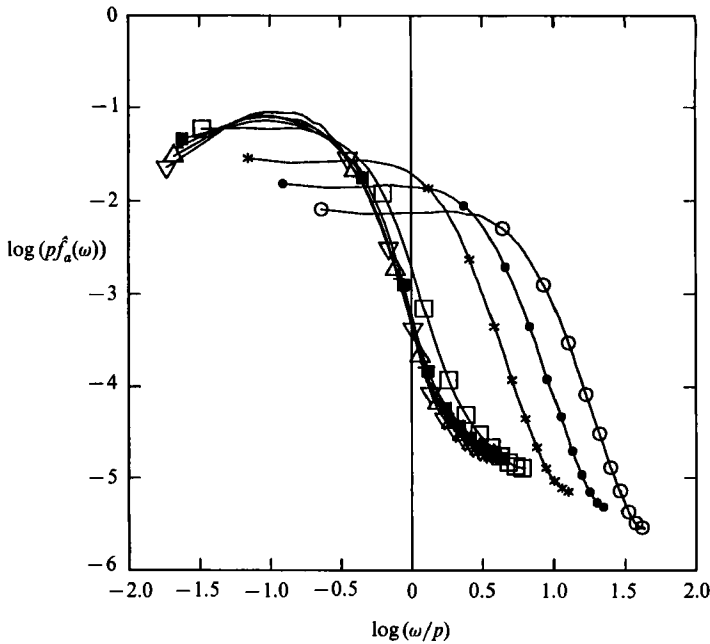


FIGURE 3. Scaled spectra of strain rate: $\log(pf_a(\omega))$ vs. $\log(\omega/p)$: $p = \frac{1}{2}$ (\circ), $p = \frac{1}{2}$ (\bullet), $p = 1$ (\ast), $p = 4$ (\square), $p = 8$ (\blacksquare), $p = 12$ ($+$), $p = 16$ (\triangle), $p = 32$ (∇).

3.1.2. Spectrum of strain rate

The frequency spectrum is the Fourier transform of the temporal autocovariance and highlights the various timescales of the random process in question. The frequency spectrum of the tangential strain rate following a propagating surface element is

$$\hat{f}_a(\omega) = \frac{\text{var}(a)}{2\pi} \int_{-\infty}^{\infty} f_a(t) e^{i\omega t} dt. \quad (32)$$

For small propagation velocities when the crossing trajectories effect is negligible, the spectrum of propagating elements is likely to be close to that of material elements. The behaviour of the spectrum at high propagation velocities can be surmized by substituting (29) in (32) leading to

$$\hat{f}_a(\omega) = \frac{\text{var}(a)}{2\pi p} \hat{F}_a\left(\frac{\omega}{p}\right), \quad (33)$$

where, $\hat{F}_a(\lambda)$ is the Eulerian wavenumber spectrum of the velocity gradient $\partial U_3/\partial x_3$.

In figure 3, the scaled spectrum ($pf_a(\omega)$) is plotted against scaled frequency ω/p on a log-log scale for various propagation velocities. The power content of the spectrum at a given propagation velocity is given by the variance of a at that value of p (plotted in figure 1). Referring to figures 1, 3 and equation (33), the effects of propagation on the spectrum can be summarized as follows:

(i) In the low propagation velocity range ($p \sim 1$, when the crossing trajectories effect becomes significant), the power content of the spectrum diminishes with increasing p . At large propagation velocities ($p \gg 1$) the power content is approximately constant. The variance of the tangential strain rate a at this limit tends asymptotically to the Eulerian variance of $\partial U_3/\partial x_3$.

(ii) The frequency of the power-containing band increases with propagation velocity.

(iii) The bandwidth of the power-containing frequencies increases with propagation velocity. At large velocities the increase in the bandwidth is linear. Although the scaled spectra collapse to a self-similar shape (figure 3) it can be seen from (33) that as propagation velocity tends to infinity the unscaled spectra will have infinite bandwidth.

3.2. Fluid velocity statistics

It was mentioned in §1 that energy is added isotropically at low wavenumbers to maintain the turbulence statistically stationary. This raises the question of the legitimacy of the use of the velocity field thus generated to study fluid velocity statistics which are large-scale phenomena. Yeung & Pope (1989) find that although the Eulerian velocity wavenumber spectrum is unphysical due to forcing, the Lagrangian velocity frequency spectrum is realistic; and conclude that the use of this velocity field to study Lagrangian statistics is valid. We use the same justification for this study.

The time-averaged kinetic energy (adjusted to account for the global fluctuations of kinetic energy, see Appendix A), and the variance of U_3 following the elements at the statistically steady state are plotted against various propagation velocities (normalized by the turbulence intensity u') in figure 4(a). The fairly large fluctuations in the statistics at small propagation velocities is due to statistical error arising for the reasons detailed in Appendix A. Despite the statistical errors it can be seen that the decrease in $\langle \text{var}(U_3) \rangle$ from Lagrangian values is monotonic. The same plot on a log-log scale (figure 4b) indicates that the transition from Lagrangian values is appreciable only at propagation velocities larger than the turbulence intensity ($p > u'$) compared to $p > v_\eta$ for strain-rate statistics. This is because there exists a range of propagation velocities ($1 < p < u'$) for which the crossing trajectories effect is negligible for large-scale phenomena (e.g. fluid velocity) but significant for small-scale phenomena (e.g. strain rate).

3.2.1. Autocorrelation of fluid velocity.

The autocorrelation function $f_u(t')$ and the correlation timescale Θ_u of the velocity process are defined (similarly to those of a) as

$$f_u(t') = \frac{1}{\text{var}(U_3)} \langle [U_3(t) - \langle U_3 \rangle][U_3(t+t') - \langle U_3 \rangle] \rangle, \quad (34)$$

and

$$\Theta_u = \int_0^\infty |f_u(t')| dt'. \quad (35)$$

Again, at high propagation velocities,

$$f_u(t') = F_u(pt'), \quad (36)$$

where $F_u(pt')$ is the longitudinal velocity spatial autocorrelation in isotropic turbulence. Further,

$$\Theta_u = \frac{1}{p} A_u, \quad (37)$$

where A_u is the longitudinal correlation lengthscale of velocity in isotropic turbulence.

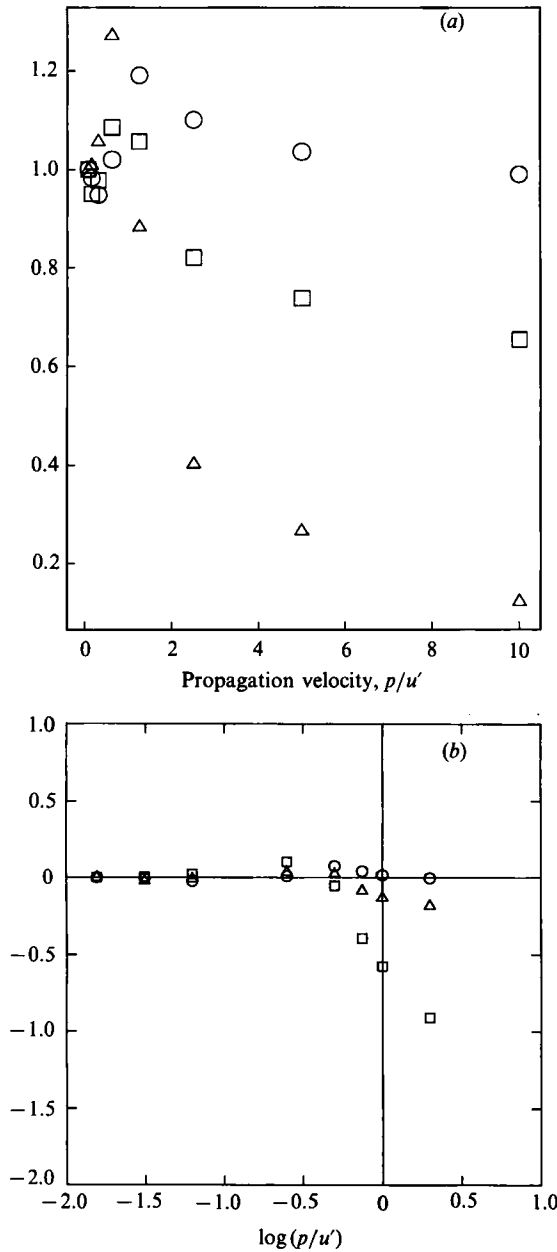


FIGURE 4. Fluid velocity statistics vs. propagation velocity: (a) linear-linear plot. $\langle U_i U_i \rangle(p) / \langle U_q U_q \rangle(0)$ (\circ), $\text{var}(U_3)(p) / \text{var}(U_3)(0)$ (\square) and $\Theta_u(p) / \Theta_u(0)$ (\triangle); (b) log-log plot: $\langle U_i U_i \rangle(p) / \langle U_q U_q \rangle(0)$ (\circ), $\text{var}(U_3)(p) / \text{var}(U_3)(0)$ (\triangle) and $\Theta_u(p) / \Theta_u(0)$ (\square). In the above $\langle U_q U_q \rangle(0) = 30.28$, $\text{var}(U_3)(0) = 9.25$ and $\Theta_u(0) = 3.55$.

The variation of Θ_u with p is plotted in figure 4(a, b). The deviation from the Lagrangian value is again monotonic and is proportional to p^{-1} at large values of the propagation velocities as indicated by (37). The autocorrelation function $f_u(t)$ in scaled time t/Θ_u is presented in figure 5 for various propagation velocities. Except for the $p = 8$ case which shows a slight deviation, the other curves collapse, indicating that $f_u(t')$ may be self-similar in this scaled time.

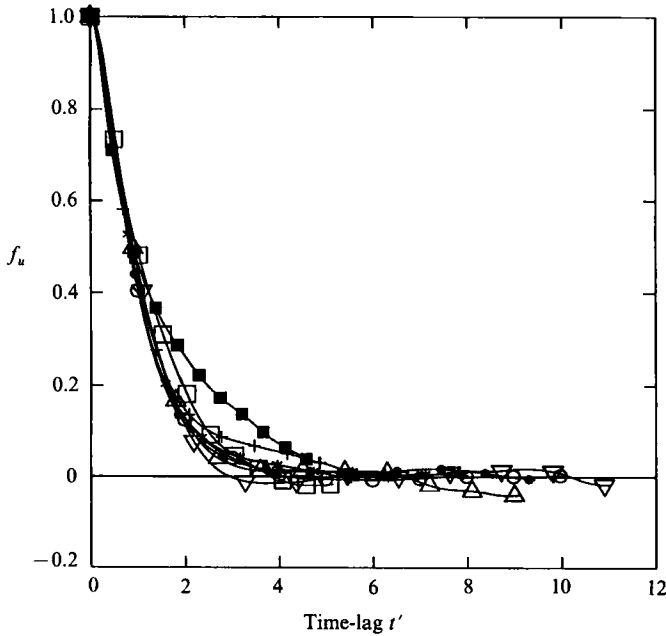


FIGURE 5. Autocorrelation of fluid velocity in scaled time: $p = 4(\circ)$, $p = \frac{1}{2}(\bullet)$, $p = 1(\ast)$, $p = 4(\square)$, $p = 8(\blacksquare)$, $p = 12(+)$, $p = 16(\triangle)$, $p = 32(\nabla)$.

3.2.2. Spectrum of fluid velocity

The frequency spectrum of the fluid velocity following a propagating surface element is

$$\hat{f}_u(\omega) = \frac{\text{var}(U_3)}{2\pi} \int_{-\infty}^{\infty} f_u(t) e^{i\omega t} dt. \tag{38}$$

For large propagating velocities this can be approximated by

$$\hat{f}_u(\omega) = \frac{\text{var}(U_3)}{2\pi p} \hat{F}_u\left(\frac{\omega}{p}\right), \tag{39}$$

where $\hat{F}_u(\lambda)$ is the Eulerian wavenumber spectrum of the velocity U_3 . In figure 6, scaled velocity spectrum ($p\hat{f}_u(\omega)$) is plotted against ω/p on a log-log scale for various propagation velocities. For high p the spectra scale as indicated by (39).

3.3. Strain rate – fluid velocity correlation

The cross-correlation function between strain rate and velocity is given by

$$f_{ua}(t') = \frac{1}{[\text{var}(U_3) \text{var}(a)]^{\frac{1}{2}}} \langle [(U_3(t) - \langle U_3 \rangle) [a(t+t') - \langle a \rangle]] \rangle. \tag{40}$$

Using similar arguments as before it can be shown that for large propagating velocities

$$f_{ua}(t') = F_{ua}(pt'), \tag{41}$$

where F_{ua} is the Eulerian spatial cross-correlation between U_3 and $\partial U_3/\partial x_3$. This cross-correlation is related to the Eulerian velocity correlation $F_u(x'_3)$ by

$$F_{ua}(x'_3) = \frac{d}{dx'_3} F_u(x'_3), \tag{42}$$

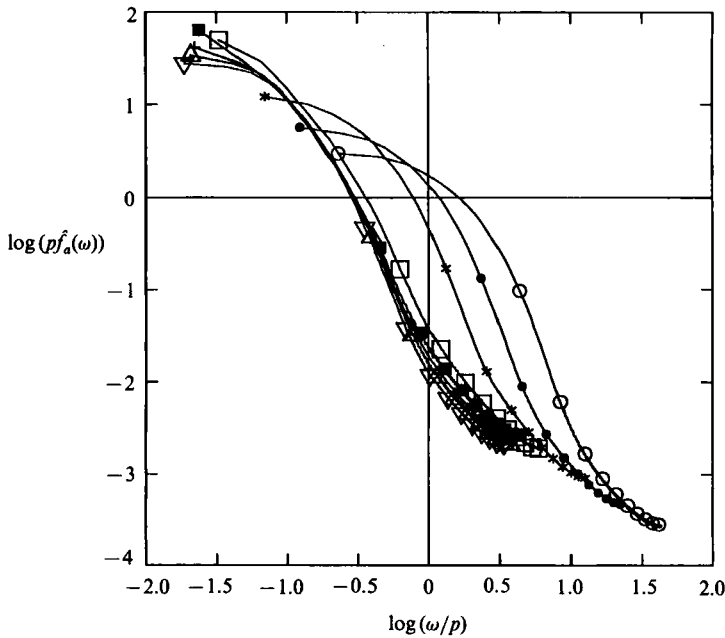


FIGURE 6. Scaled spectra of fluid velocity $\log(pf_a^\omega)$ vs. $\log(\omega/p)$: $p = \frac{1}{4}$ (\circ), $p = \frac{1}{2}$ (\bullet), $p = 1$ ($*$), $p = 4$ (\square), $p = 8$ (\blacksquare), $p = 12$ ($+$), $p = 16$ (\triangle), $p = 32$ (∇).

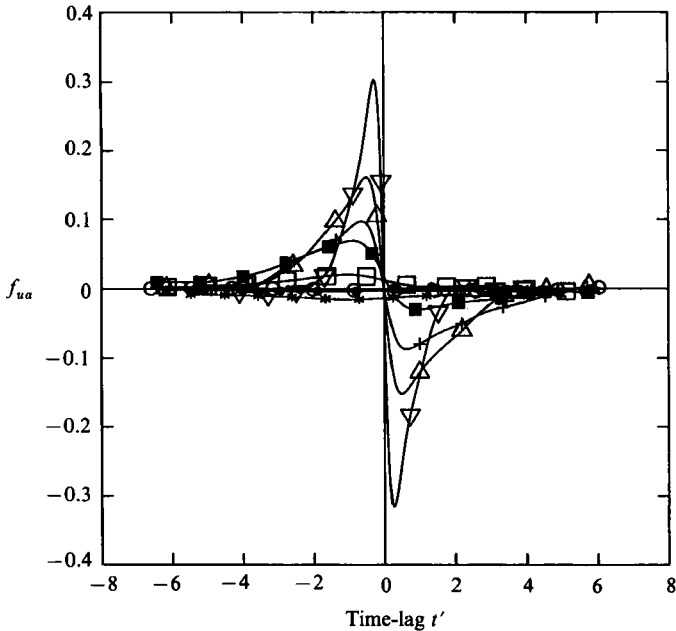


FIGURE 7. Cross-covariance of fluid velocity and strain rate: $p = \frac{1}{4}$ (\circ), $p = \frac{1}{2}$ (\bullet), $p = 1$ ($*$), $p = 4$ (\square), $p = 8$ (\blacksquare), $p = 12$ ($+$), $p = 16$ (\triangle), $p = 32$ (∇).

where $x'_3 = pt'$. Since $F_u(x'_3)$ is a symmetric function in x'_3 about the origin, $F_{ua}(x'_3)$ is antisymmetric about the origin.

In figure 7 the cross-correlation is plotted against time for various propagation velocities. Fluid velocity and strain rate are poorly correlated at low p . With

increasing propagation velocity the curves get narrower and within the narrow band the correlation increases. At high values of p the shape of the cross-covariance approaches the antisymmetric shape suggested by (42).

4. Evolution of curvature

The statistics considered so far depend only upon the first derivative of velocity following the propagating element. The curvature, on the other hand, is a function also of the second derivatives. Referring to §1.3, the characteristic curvature $C(t)$ (≥ 0) evolves according to (12), where b_1, b_2 and b_3 are stationary random variables. It is instructive to look at the exact solution to the curvature equation when b_1, b_2 and b_3 are constants and $C(0) = 0$.

For the case of $b_3 = 0$ (material element)

$$C(t) = (b_1/b_2) [e^{b_2 t} - 1]; \tag{43}$$

for the case of $(4b_1 b_3 - b_2^2) \equiv y^2 > 0$

$$C(t) = \left(\frac{y}{2b_3} \right) \frac{y \tan(\frac{1}{2}t) + b_2}{y - b_2 \tan(\frac{1}{2}yt)} - \frac{b_2}{2b_3}; \tag{44}$$

for the case of $(b_2^2 - 4b_1 b_3) \equiv z^2 > 0$

$$C(t) = 2b_1 \frac{e^{zt} - 1}{b_2 + z - (b_2 - z)e^{zt}}; \tag{45}$$

and when $(b_2^2 - 4b_1 b_3) = 0$

$$C(t) = \frac{b_2^2 t}{2b_3(2 - b_2 t)}. \tag{46}$$

We now use the above solutions to explore the possibility of the curvature becoming infinite in finite time. For this analysis, only positive values of b_1 and non-negative values of b_3 are meaningful. The bending term b_1 must certainly be positive initially for it is this term that causes the curvature to go from zero to positive values. Since we are interested in the situation when propagation does not decrease curvature, (referring to (12)) b_3 must be non-negative.

Case (i): $b_2 > 0; b_3 = 0$. The curvature grows exponentially in time and hence is finite for all finite time.

Case (ii): $b_2 < 0; b_3 = 0$. For this combination of parameters the curvature asymptotes to a steady-state value of

$$C(\infty) = b_1/|b_2|. \tag{47}$$

So for material surfaces the curvature grows exponentially or attains steady-state value and hence cusps do not form in finite time. In Girimaji (1991) it is shown that in stationary, isotropic turbulence, the curvature of material elements goes to a stationary distribution.

Case (iii): $b_2 > 0; z^2 \equiv (b_2^2 - 4b_1 b_3) > 0$. For this case singularity will be reached at time t_* given by

$$t_* = \frac{1}{z} \ln \frac{b_2 + z}{b_2 - z}. \tag{48}$$

Case (iv): $b_2 > 0; (b_2^2 - 4b_1 b_3) = 0$. The curvature becomes infinite at

$$t_* = 2/b_2. \tag{49}$$

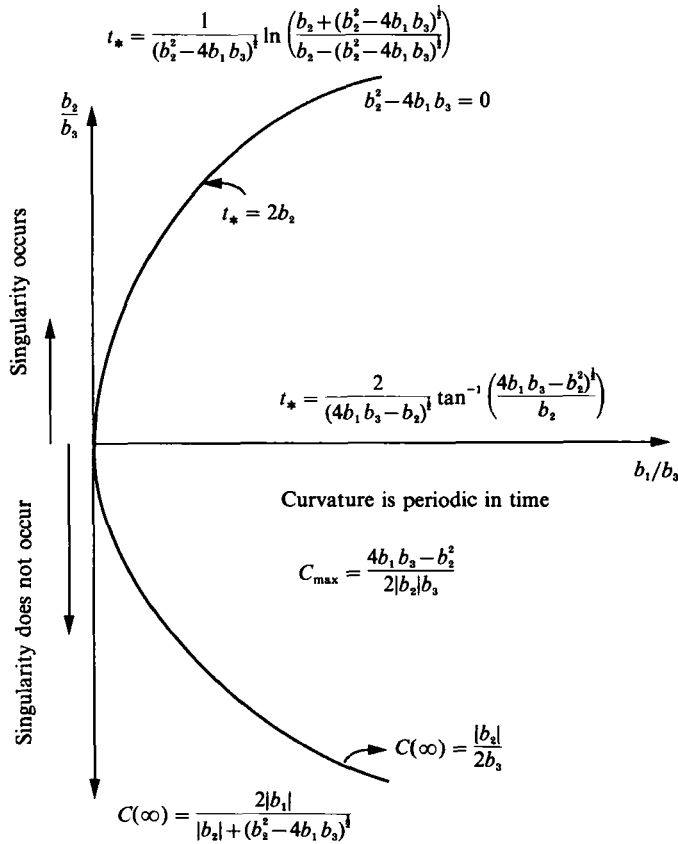


FIGURE 8. Regimes of cusp formation: various ranges b_1 , b_2 and b_3 .

Case (v): $b_2 > 0$; $y^2 \equiv (4b_1b_3 - b_2^2) > 0$. This combination of the coefficients also leads to cusp formation at

$$t_* = \frac{2}{y} \tan^{-1} \frac{y}{b_2}. \tag{50}$$

Case (vi): $b_2 < 0$; $y^2 \equiv (4b_1b_3 - b_2^2) > 0$. For this case the curvature is periodic in time but always finite. The maximum value attained by the curvature is given by

$$C_{\max} = \frac{y}{2|b_2|b_3}. \tag{51}$$

Case (vii): $b_2 < 0$; $(b_2^2 - 4b_1b_3) = 0$. With this combination of coefficients, at large times the curvature asymptotes to

$$C(\infty) = |b_2|/2b_3. \tag{52}$$

Case (viii): $b_2 < 0$; $z^2 \equiv (b_2^2 - 4b_1b_3) > 0$. Again the curvature does not go to infinity, and at large times asymptotes to

$$C(\infty) = \frac{2b_1}{|b_2| + z}. \tag{53}$$

These observations are summarized in figure 8. So it is clear that for cusp formation in finite time the stretching coefficient b_2 and the propagation coefficient

b_3 must be positive. In other words the flow field should compress the surface rather than stretch it. In turbulence, although any surface element is stretched on average, it also experiences compressive strain for about 30% of the time (Girimaji & Pope 1990; Yeung *et al.* 1990). So the behaviour of characteristic curvature in turbulence is not clear.

In a turbulent velocity field, the characteristic curvature is a non-negative random process $\{C(t); 0 \leq t \leq t_*\}$ with the initial condition $C(0) = 0$; t_* is the time the process takes to attain infinity. Clearly t_* is a random variable which may be finite with non-zero probability. Hence the study of evolution of the moments in time is not meaningful since the moments may cease to exist beyond a certain time. A more useful approach then is the characterization of an associated random variable, *hitting time*, $L(C)$. The hitting time – denoted by $L(c)$ – to the level c , of the random process $C(t)$, represents the first time the random process attains the value c . The formal definition of the hitting time to the level c of the i th realization, $C_i(t)$, of the random process is

$$L_i(c) = \inf\{t \geq 0; C_i(t) \geq c\}. \quad (54)$$

From its definition following properties of the hitting time can be inferred.

(i) In statistically stationary, homogeneous, isotropic turbulence the hitting times for various realizations (surface elements) are identically distributed random variables with the probability distribution being a function of the level c .

(ii) If $c_2 > c_1$ then

$$L_i(c_1) \leq L_i(c_2). \quad (55)$$

(iii) The time taken for cusp formation is the hitting time of level infinity, $L_i(\infty)$. So if for a particular realization a cusp forms in finite time then the hitting time of all the levels of c are finite.

From an ensemble of I realizations the mean hitting time to a level c can be estimated by

$$\langle L(c) \rangle = \frac{1}{I} \sum_{i=1}^I L_i(c). \quad (56)$$

While it seems intuitively plausible that $\langle L(c) \rangle$ is finite for small curvatures the existence of the mean hitting time for large curvature levels is not evident.

To resolve the issue of the existence of the mean hitting time for large curvatures, appeal is made to the DNS data. At time $t = 0$, $I = 8192$ plane surface elements are released in stationary, isotropic turbulence and their curvatures calculated (see §2 for more details). It is found that, for all propagation velocities considered, a large fraction of the surface elements form cusps before the end of the simulation. This is in direct contrast to the conclusions of Ashurst *et al.* (1988); the contradiction is addressed in detail in Appendix B. To quantify our results two statistics are introduced: $n(t)$, the fraction of surface elements that are non-singular at time t ; and $T_{\frac{1}{2}}$, the time at which $n(t) = \frac{1}{2}$. The relevance of these statistics is easily understood from the following relationships:

$$\text{Prob}\{t_* > t\} = n(t), \quad (57)$$

and

$$\text{Prob}\{t_* > T_{\frac{1}{2}}\} = \frac{1}{2}. \quad (58)$$

The probability density function (p.d.f.) of t_* , $f_{t_*}(t)$, can be derived in terms of $n(t)$ from (57):

$$f_{t_*}(t) = -\frac{d}{dt} n(t). \quad (59)$$

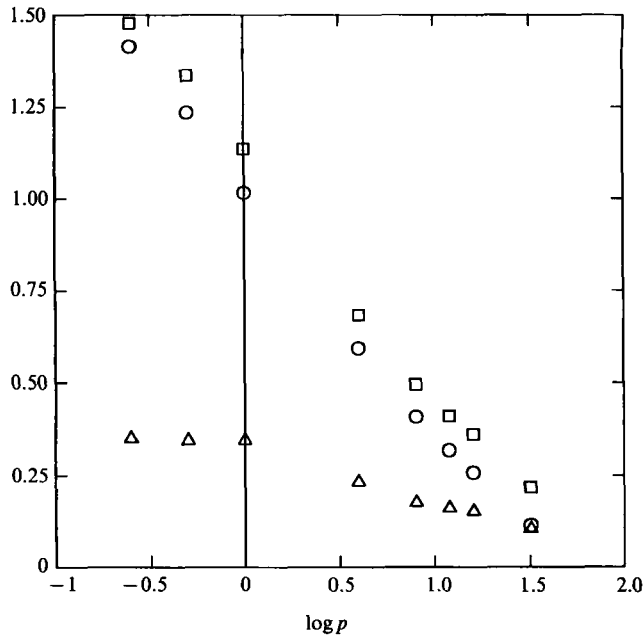


FIGURE 9. Curvature statistics vs. propagation velocity (log-log plot): $T_{\frac{1}{2}}$ (○), t_{fp} (□), $\langle H(10) \rangle$ (△).

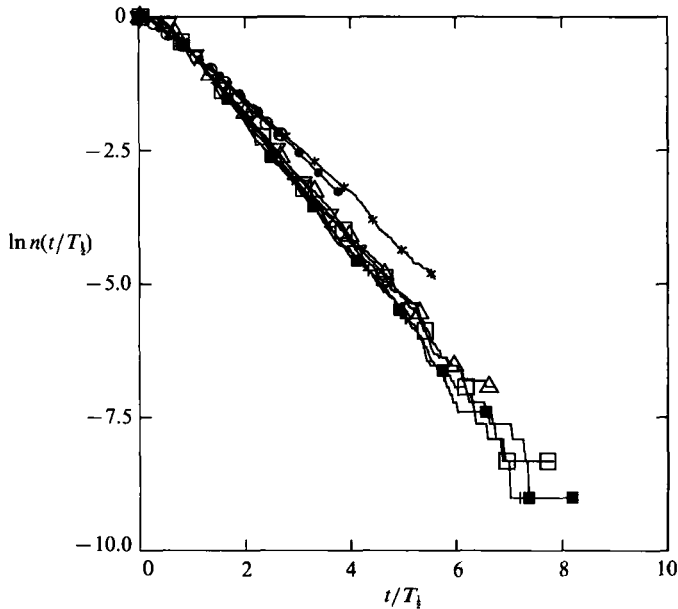


FIGURE 10. Fraction of non-singular elements in scaled time $\ln n(t/T_{\frac{1}{2}})$ vs. $t/T_{\frac{1}{2}}$: $p = \frac{1}{2}$ (●), $p = \frac{1}{2}$ (●), $p = 1$ (*), $p = 4$ (□), $p = 8$ (■), $p = 12$ (+), $p = 16$ (△), $p = 32$ (▽).

In figure 9, the timescale $T_{\frac{1}{2}}$ is presented as a function of the propagation velocity p on a log-log scale. No power-law dependence of $T_{\frac{1}{2}}$ on p over the entire range is evident although at high values of p , $T_{\frac{1}{2}}$ appears to scale as $p^{-0.5}$. In figure 10, $n(t)$ is plotted as a function of $t/T_{\frac{1}{2}}$ on a log-linear scale, for various propagation velocities.

For the two smallest velocities the values of n at the end of the simulations ($t = t_{fp}$) are both approximately 0.1, whereas for the other velocities $n(t_{fp})$ goes down very close to zero. At large p -values the curves nearly collapse on one another. The most important observation is that for all propagation velocities the $\log n(t) - (t/T_{\frac{1}{2}})$ curves are nearly linear with approximately -1 slopes at large values of scaled time. This observation in conjunction with (59) suggests the following behaviour of $f_{t_*}(t)$ at large values of $t/T_{\frac{1}{2}}$:

$$f_{t_*}(t/T_{\frac{1}{2}}) \sim e^{-t/T_{\frac{1}{2}}}. \tag{60}$$

The important consequences of (60) are:

(i) All propagating elements (in the range of velocities considered) form cusps in finite time with probability nearly one. More precisely, for any given ϵ , however small, there exists a finite time $t_{*\epsilon}$ such that

$$\text{Prob} \{t_* < t_{*\epsilon}\} \geq 1 - \epsilon, \tag{61}$$

where

$$t_{*\epsilon} \sim \ln(T_{\frac{1}{2}}/\epsilon). \tag{62}$$

(ii) For any propagation velocity, if $T_{\frac{1}{2}}(p)$ is finite then all finite moments of $t_*(=L(\infty))$ exist since, for all $0 < n < \infty$,

$$\langle t_*^n(p) \rangle \sim \frac{1}{T_{\frac{1}{2}}} \int_0^\infty t_*^n e^{-t_*/T_{\frac{1}{2}}} dt_* \sim T_{\frac{1}{2}}^n(p) \Gamma(n+1) < \infty. \tag{63}$$

(iii) All moments of $L(c)$ exist for all finite c since, for any n ,

$$\langle L^n(c) \rangle \leq \langle L^n(\infty) \rangle < \infty. \tag{64}$$

The characteristic radius of curvature $R(t)$ is also a non-negative random process with the initial condition $R(0) = \infty$. Analogous to $L(c)$ a hitting time $H(r)$ for the $R(t)$ process is defined as

$$H(r) = \inf\{t \geq 0; R(t) \leq r\}. \tag{65}$$

It is easy to derive the following relationship between the hitting times of the two processes:

$$H(r) = L(1/r). \tag{66}$$

At large curvatures the rate of change of radius of curvature is nearly a constant (see (13)) and hence $H(r)$ can be expected to be a linear function of r . Hence in the investigation of cusp formation it is preferable to consider $H(r)$ rather than $L(c)$ which is less tractable in this range of curvature. In the remainder of this Section the behaviour of the mean hitting time $\langle H(r) \rangle$ of the $R(t)$ process for various propagation velocities is discussed. Then the shape of the surface element and the stretching and straining experienced by it are presented.

4.1. Mean hitting time $\langle H(r) \rangle$

As was mentioned earlier in this section, the length of the simulation is smaller than the time taken for all the surface elements to attain singularity. The estimate $\langle H^e(r) \rangle$ of the mean hitting time $\langle H(r) \rangle$ is then calculated according to

$$\langle H^e(r) \rangle = \frac{1}{I} \sum_{i=1}^I \min \{H_i(r), t_{fp}\}, \tag{67}$$

where, t_{fp} is the length of the simulation (see §2, (16)). This is a meaningful estimate if t_{fp} is large enough to capture all the essential features of the curvature evolution.

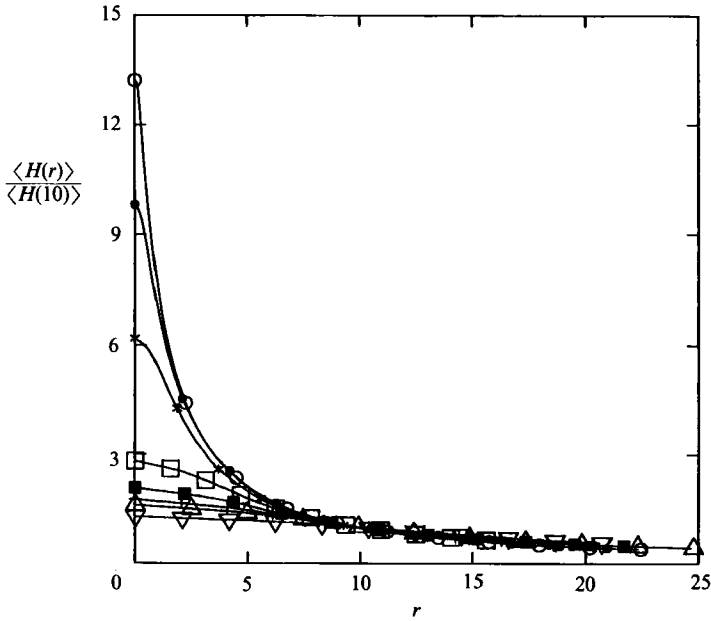


FIGURE 11. Mean hitting time *vs.* characteristic radius: $p = \frac{1}{4}$ (\circ), $p = \frac{1}{2}$ (\bullet), $p = 1$ ($*$), $p = 4$ (\square), $p = 8$ (\blacksquare), $p = 12$ ($+$), $p = 16$ (\triangle), $p = 32$ (∇).

Even for the smallest propagation velocity t_{fp} is such that over 90% of the elements attain singularity and hence t_{fp} is considered large enough.

In figure 9, the time taken for the characteristic curvature to decrease from infinity to 10η , $\langle H(10) \rangle$, is provided for various propagating velocities. Unlike $T_{\frac{1}{2}}$, $\langle H(10) \rangle$ is nearly constant at small propagation velocities. This is perhaps because at radii larger than 10η the curvature evolves mostly due to bending (term of $O(1)$) and stretching (term of order $O(1/R)$) (equation (12)). The effect of propagation (term of $O(1/R)^2$) is felt only through the shortened timescales of the bending and stretching processes. In figure 11, the scaled mean hitting time ($\langle H(r) \rangle / \langle H(10) \rangle$) is plotted as a function of the characteristic radius of curvature r for various propagation velocities. For radii greater than 10η the curves for various p -values nearly collapse to a single line. In this regime of radius, bending and stretching are the important processes and the implication of the collapse of the curves is that these processes scale similarly for various propagation velocities. In the small-radii regime, however, the curves of various propagation velocities diverge. In this regime propagation is the important curvature-producing mechanism and hence scaling with $\langle H(10) \rangle$, which represents the bending-stretching processes, does not collapse the curves.

In the small-radii regime, the behaviour of the mean hitting time can be estimated using (13) to be,

$$\frac{d\langle H(r) \rangle}{dr} \sim \frac{1}{p}. \quad (68)$$

At large radius of curvature the evolution equation of R can be approximated to

$$dR/dt \approx b_1 R^2. \quad (69)$$

and hence,

$$\frac{d\langle H(r) \rangle}{dr} \sim \frac{1}{\langle b_1 \rangle r^2}. \quad (70)$$

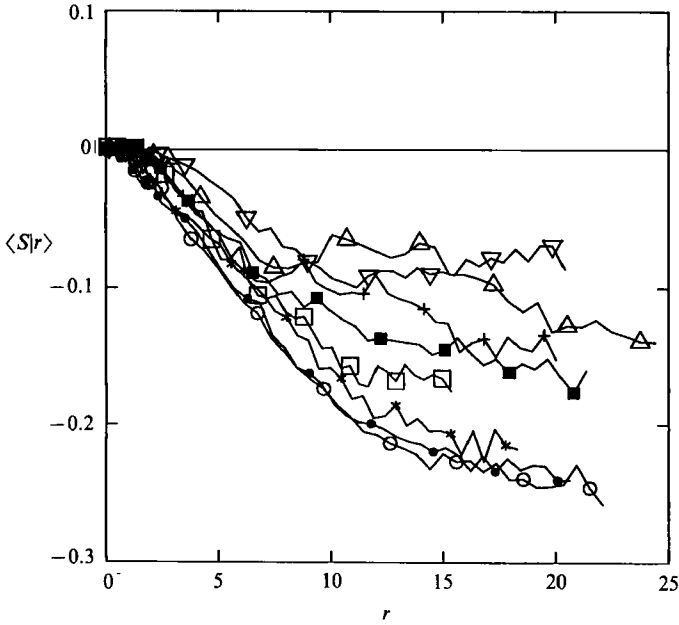


FIGURE 12. Shape factor vs. characteristic radius: $p = \frac{1}{4}$ (\circ), $p = \frac{1}{2}$ (\bullet), $p = 1$ ($*$), $p = 4$ (\square), $p = 8$ (\blacksquare), $p = 12$ ($+$), $p = 16$ (\triangle), $p = 32$ (∇).

A plot of $(p d\langle H(r) \rangle / dr)$ vs. r on a log-log scale for various propagation velocities (not given) indeed shows that the scaling is as indicated by (68) and (70) is the limits of small and large radii respectively.

4.2. Shape of the surface element

The shape factor S of a surface element is defined as,

$$S \equiv k_2/k_1, \quad (71)$$

where k_2 and k_1 are the smaller and the larger in absolute value of the principal curvatures of the surface element (§1.2). By definition S lies between -1 and $+1$ with values 0 , 1 and -1 corresponding to cylindrical, spherical and pseudospherical shapes respectively. The conditional expectation of S for a given radius curvature r – denoted by $\langle S|r \rangle$ – is presented in figure 12 for various propagation velocities. The observations from the figures are: (i) Highly curved elements are almost completely cylindrical in shape. (ii) Mildly curved elements are also cylindrical in shape, though tending more towards pseudospherical than highly curved elements. The above two observations are consistent with the findings of Pope *et al.* (1989) for material surfaces. (iii) With increasing propagation velocity the surface elements tend to be more cylindrical than pseudospherical for the entire range of the radius of curvature.

4.3. Straining of propagating surface

It was seen in the previous Section that with increasing propagation velocities the mean strain rate experienced by the surface elements decreases monotonically from positive to near zero values. In this subsection the strain rate conditioned upon curvature is studied. In figure 13 $\langle a|r \rangle$ is presented for various propagation velocities.

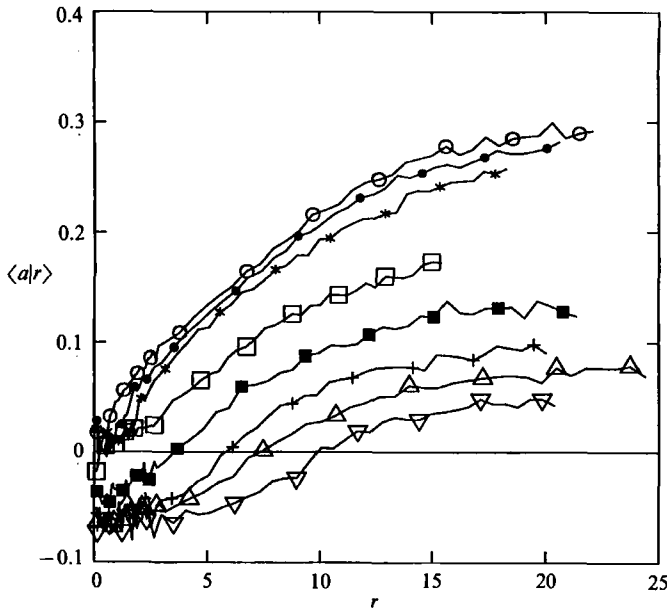


FIGURE 13. Strain rate vs. characteristic radius: $p = \frac{1}{4}$ (\circ), $p = \frac{1}{2}$ (\bullet), $p = 1$ ($*$), $p = 4$ (\square), $p = 8$ (\blacksquare), $p = 12$ ($+$), $p = 32$ (\triangle), $p = 32$ (∇).

The near-zero average straining experienced by highly curved slowly propagating surfaces can be explained by the fact that the high curvatures are the effect rather than cause. High curvatures tend to develop in surface elements that experience less positive strain rates. A similar explanation is valid for the negative strain rates experienced by the highly curved rapidly propagating elements. When a rapidly propagating element experiences negative strain rate (positive b_2) the curvature increases due to straining of the surface. If the resulting curvature is large enough, propagation becomes the dominant curvature-producing mechanism, curving the surface rapidly to a singularity before the strain rate changes significantly. Hence the expectation of strain rate conditioned upon small radii is negative.

4.4. *Stretching of propagating surface*

In figure 14, the conditional expectation of the area ratio $\langle \ln(A) | r \rangle$ is plotted against characteristic curvature r for various propagation velocities. The observations are: (i) The mean area ratio increases with the radius of curvature. At small radii $\ln A$ decreases linearly with $\ln R$. (ii) With increasing propagation velocity, curves shift to lower and lower values of $\ln A$. Indeed the mean of $\ln A$ of highly curved rapidly propagating surfaces is negative, indicating that highly curved elements shrink in size. Remember that $\ln A(t) = 0$ corresponds to the surface area of the element at time t being the same as that at the initial time.

The linear relation between $\ln A$ and $\ln R$ at small radii is easily explained. The evolution equation of $\ln A$ (equation (11)) of highly curved elements can be approximated to

$$d \ln A / dt = -p/R. \tag{72}$$

When combined with (13) this leads to

$$d \ln A / d \ln R = 1. \tag{73}$$

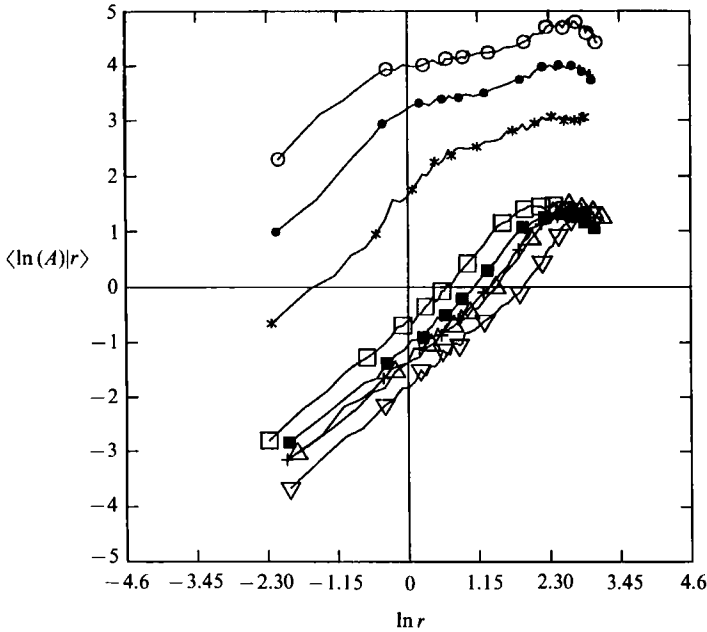


FIGURE 14. Area ratio vs. characteristic radius: $p = \frac{1}{4}$ (\circ), $p = \frac{1}{2}$ (\bullet), $p = 1$ ($*$), $p = 4$ (\square), $p = 8$ (\blacksquare), $p = 12$ ($+$), $p = 16$ (\triangle), $p = 32$ (∇).

5. Summary

In this paper the evolution of infinitesimal surface elements propagating passively in isotropic turbulence is studied using a velocity field generated by direct numerical simulations. The Taylor-scale Reynolds number of the turbulence is 37. Evolution equations of the surface-normal N , characteristic curvature C , and area ratio A (defined in §1.2) are solved using second-order-accurate predictor-corrector schemes (described in §2). The behaviour of tangential strain rate, fluid velocity and characteristic curvature are studied. The following is a summary of the results.

(i) The values of the mean and variance of the tangential strain-rate-following propagating elements go from Lagrangian values at low propagation velocities to the corresponding Eulerian values at high velocities. The transition appears monotonic and the deviation from Lagrangian values is noticeable only for propagation velocities greater than v_η (figure 1). Slowly propagating surfaces experience positive strain rates on average, whereas the mean strain rate experienced by rapidly propagating elements is nearly zero.

(ii) The strain-rate autocorrelation function is mostly positive at low propagation velocities (similar to the material-element autocorrelation presented in Yeung *et al.* 1990), but has a large negative loop (characteristic of the Eulerian spatial velocity-gradient correlation) at high velocities (figure 2). At high propagation velocities, the frequency spectrum of the strain rate assumes a self-similar form which can be related to the Eulerian velocity-gradient wavenumber spectrum (figure 3).

(iii) The one-time statistics of fluid velocity also go monotonically from Lagrangian to Eulerian values with increasing propagation velocity. The deviation from the Lagrangian values is discernable only for propagation velocities greater than $u' = 3.2v_\eta$ (figure 4).

(iv) The fluid-velocity autocorrelation function for various propagation velocities appear self-similar when the time lag is scaled with the velocity correlation

timescales (figure 5). At high propagation velocities the spectra assume a self-similar form that can be related to the Eulerian velocity wavenumber spectrum (figure 6).

(v) Initially plane propagating surface elements develop cusps with probability nearly one in finite time (figure 10). The time taken for cusp formation decreases with increasing propagation velocities approximately as $p^{-0.5}$ (figure 9).

(vi) The evolution of curvature is studied using the concept of *hitting time* (figure 11).

(vii) The shape of the propagating element is nearly cylindrical. Mildly curved slowly propagating elements tend to be more pseudospherical than highly curved rapidly propagating elements (figure 12).

(viii) Milder curvatures are associated with positive mean strain rates and higher curvatures with zero or negative mean strain rates (figure 13).

(ix) Mildly curved elements are associated with larger surface areas than highly curved elements (figure 14).

The above conclusions are valid for surface elements propagating passively at constant velocity in isotropic turbulence. Although these results cannot be generalized literally to flamelets, the knowledge gleaned here can go a long way in helping us better understand flamelet behaviour in turbulence.

5.1. Behaviour at high Reynolds numbers

The behaviour of propagating surface elements at higher Reynolds numbers is likely to be qualitatively similar to that presented in this paper. The strain-rate statistics are likely to scale with the Kolmogorov scales and the fluid velocity statistics with the turbulence intensity and the integral time- and lengthscales. This can be confirmed only by performing the preceding study for various Reynolds numbers. Surely at the limits of low and high propagation velocities the statistics should scale in fashions similar to those presented in this paper. With increasing separation of scales the range of propagation velocities for which the crossing trajectories effect is important for small-scale statistics but negligible for large-scale statistics will increase.

This work was supported by the US Air Force Office of Scientific Research (grant number AFOSR-88-0052). Computations conducted during the research were performed on the Cornell National Supercomputer Facility, which is supported in part by the National Science Foundation, New York State, the IBM Corporation and the members of the Corporate Research Institute.

Appendix A. Accounting for the global fluctuations of statistics

With increasing Reynolds numbers the separation between the large and small scales gets larger. As the Reynolds number becomes higher, the energy-containing scales of large-scale quantities (e.g. velocity) get closer and closer to the scales at which energy is input to maintain statistical stationarity (Eswaran & Pope 1987). At these high Reynolds numbers the global statistics of the large-scale quantities fluctuate, owing both to the effect of forcing wavenumbers close to the energy-containing range; and to the fact that the integral lengthscale of turbulence becomes comparable to the size of the computational domain. Yeung & Pope (1989) found this to be the case for $R_\lambda = 93$ simulation on a 128^3 grid.

In this work (64^3 simulation of $R_\lambda = 37$) it is found that the Eulerian statistics of large-scale quantities (e.g. $\langle u_i u_i \rangle$) fluctuate. As in the case of Yeung & Pope (1989)

the Lagrangian statistics (of kinetic energy in the present case) are corrected to account for these global fluctuations as follows:

$$\langle u_i u_i \rangle_{\text{corrected}}(t) = \langle u_i u_i \rangle_{\text{uncorrected}}(t) \times \frac{\langle u_i u_i \rangle_{\text{Eulerian}}(t)}{\langle u_i u_i \rangle_{\text{Eulerian time-averaged}}}. \quad (\text{A } 1)$$

Appendix B. Validity of the curvature equations

Ashurst *et al.* (1988) report a numerical study of propagating surfaces in simple one-dimensional sinusoidal velocity fields. A conclusion of their work is that cusps do not form if the normalized propagation speed is sufficiently small – in direct opposition to the conclusion drawn from the current study. While these simple sinusoidal velocity fields are markedly different from the turbulence studied here, the different conclusions on cusp formation require further examination.

In this Appendix we re-examine the flows considered by Ashurst *et al.* using two different numerical methods. The first method is that used in the DNS calculations, based on the ordinary differential equations for infinitesimal surface elements. The second is a simple surface tracking algorithm (described below) that requires minimal algebra and coding to implement, and that consequently has a high probability of being free of human error. For the cases considered, the results of these two algorithms are in agreement; and they both agree with the analytic solution for the simplest case of a material surface. Applying these algorithms to propagating surfaces in sinusoidal velocity fields, we find that cusps form in finite time, however small the propagation velocity. This conclusion is in accord with the DNS findings reported in the text, and suggests that the numerical method used by Ashurst *et al.* is deficient.

Initially ($t = 0$) there is an infinite plane surface with $X_3(t) = 0$. The two velocity fields considered are:

$$\text{pulsating flow: } U_2(x_1, t) = u \cos(2\pi x_1) \sin(2\pi t); \quad (\text{B } 1)$$

$$\text{travelling wave: } U_2(x_1, t) = u \cos(2\pi[x_1 + t]). \quad (\text{B } 2)$$

Without loss of generality the wavelength (L) and period (T) are specified to be 2π . Hence the propagation speed w and the characteristic fluid velocity u should be thought of as being normalized by L/T . The fluid velocity is specified to be unity, leaving $w (= wT/L)$ as the only physical parameter.

The two numerical methods used to track the surface are now described.

B.1. Infinitesimal surface elements

For the cases considered, the equations for an infinitesimal surface element's properties (equations A.32–36 of Pope 1988) reduce to

$$\dot{X}_1 = wN_1, \quad \dot{X}_2 = wN_2 + U_2, \quad \dot{X}_3 = 0; \quad (\text{B } 3)$$

$$\dot{N}_1 = -N_2^3 \frac{\partial U_2}{\partial x_1}, \quad \dot{N}_2 = N_1 N_2^2 \frac{\partial U_2}{\partial x_1}, \quad \dot{N}_3 = 0; \quad (\text{B } 4)$$

and

$$\dot{k} = N_2^3 \frac{\partial^2 U_2}{\partial x_1^2} + 3kN_1 N_2 \frac{\partial U_2}{\partial x_1} + wk^2; \quad (\text{B } 5)$$

where $k = k_1$, and $k_2 = 0$. These equations are integrated numerically by a second-order-accurate predictor–corrector scheme with a time-step of $\Delta t = 0.005/(u + w)$. A

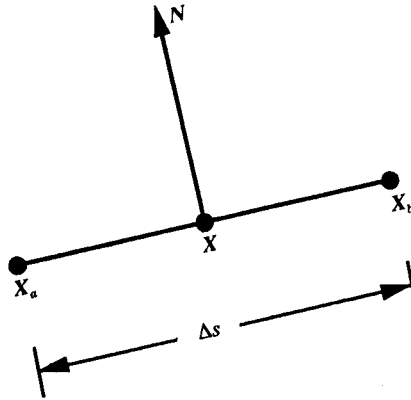


FIGURE 15. Sketch of a finite surface element.

total of 101 elements are considered which, initially, are uniformly spaced between $x_1 = 0$ and $x_1 = 1$ (i.e. one period).

The curvature equation (B 5) is integrated by a scheme similar to that described in the text, so that for large curvature the analytic solution is obtained. Cusp formation is detected as $(1/k) = 0$, and when it occurs the integration of (B 5) is discontinued. However (B 3) and (B 4) contain no singularities, and are integrated through and beyond cusp formation.

B.2. Finite surface elements

A finite surface element is sketched on figure 15: it is represented by its end points X_a and X_b , which are a distance Δs apart. The element is centred at $X = \frac{1}{2}(X_a + X_b)$, and the unit normal N is defined to be normal to the straight line joining the end points. In a time-step Δt , X_a is advanced by the second-order-accurate solution of the equation

$$\dot{X}_a = wN(t) + U(X_a, t), \tag{B 6}$$

and similarly for X_b . At the end of each time-step the element is redefined by changing its length Δs to $\Delta s_0 = 0.01$, without changing X or N . Providing the surface is regular, this numerical method for determining $X(t)$ is second-order accurate with respect to both Δs_0 and Δt .

This method is used to track 101 elements, with the same initial conditions as the infinitesimal surface elements. The curvature is obtained (prior to cusp formation) by numerically differentiating the surface, parametrized by its initial position (see do Carmo 1976, p. 25).

B.3. Results

In order to validate the numerical methods, calculations were performed for material surfaces ($w = 0$) for which analytic solutions for $X(t)$, $N(t)$ and $k(t)$ are readily obtained.

Figure 16 shows $X_2(t)$ plotted against $X_1(t)$ for the pulsating flow at $t = 7, 7\frac{1}{8}, \dots, 7\frac{7}{8}, 8$. The minimum of X_2 decreases from zero at $t = 7$ to π^{-1} at $t = 7\frac{1}{2}$, and then increases again. Each visible line is the superposition of several lines: one for the exact solution, one for each of the numerical methods, and (except at $t = 7\frac{1}{2}$) the same three lines for the second half of the period. The fact that the lines appear coincident after 7 time periods confirms the accuracy of the numerical methods.

For the travelling wave velocity field, figure 17 shows the curvature $k(t)$ as a

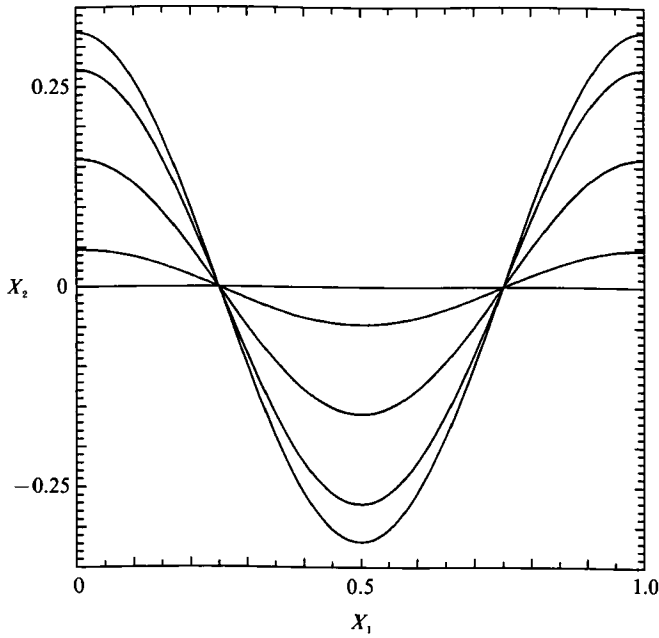


FIGURE 16. Material surface in pulsating flow: $X_2(t)$ vs. $X_1(t)$ for $t = 7, 7\frac{1}{8}, \dots, 7\frac{7}{8}, 8$. Superimposed results from (a) exact solution, (b) infinitesimal surface element method, (c) finite surface element method.

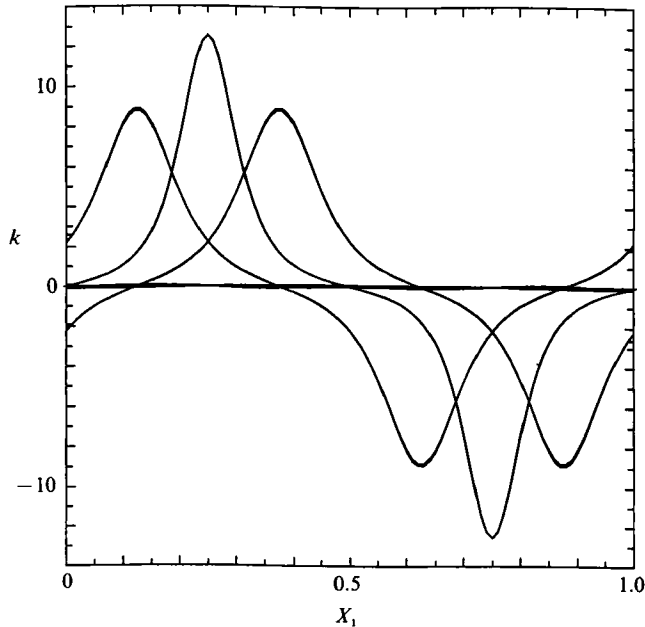


FIGURE 17. Material surface in a travelling wave: curvature $k(t)$ vs. $X_1(t)$. Same times and methods as figure 16.

function of $X_1(t)$ at $t = 7, 7\frac{1}{4}, 7\frac{1}{2}, 7\frac{3}{4}$ and 8. The surface is plane at $t = 7$ and $t = 8$; and the extremum of k moves to the left as t increases. Again, the analytic solution and the results of both numerical methods are shown. The near-coincidence of the lines confirms the accuracy of the numerical methods.

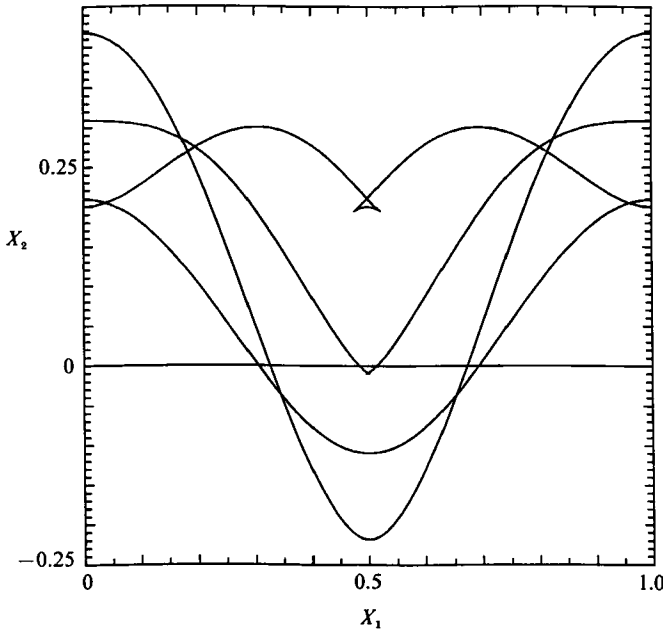


FIGURE 18. Propagating surface ($w = 0.2$) in pulsating flow: $X_2(t)$ vs. $X_1(t)$ for $t = 0, \frac{1}{4}, \frac{1}{2}, \frac{3}{4}, 1$. Superimposed results of finite and infinitesimal surface element methods.

The propagating surface with speed $w = 0.2$ in the pulsating flow is shown at $t = 0, \frac{1}{4}, \frac{1}{2}, \frac{3}{4}, 1$ in figure 18. An analytic solution has not been obtained; but, again, the near-coincidence of the curves obtained from the two numerical schemes provides confirmation of their accuracy.

A cusp forms at $X_1 = \frac{1}{2}, t = 0.708$. At $t = 1$ the two critical points arising from the cusp may be observed: the same pair exist at $t = \frac{3}{4}$, but are less clearly seen.

As might be expected from the geometry of the problem, cusp formation is found to occur always at $X_1 = \frac{1}{2}$. At this location the curvature equation (B 5) reduces, for pulsating flow, to

$$\dot{k} = (2\pi)^2 \sin(2\pi t) + wk^2. \tag{B 7}$$

It is now shown, from this equation, that a cusp forms in finite time for all propagation speeds, $w > 0$; and an upper bound is obtained for the time to cusp formation, t_* .

The sinusoidal bending term in (B 7) can be removed by considering k averaged over a cycle. To this end, for any quantity $q(t)$ we define

$$\overline{q(t)} = \int_t^{t+1} q(s) ds. \tag{B 8}$$

Integrating (B 7) between t and $t+1$ we obtain

$$(d/dt) \bar{k} = w\bar{k}^2 \geq w\bar{k}^2, \tag{B 9}$$

where the inequality follows from the observation

$$\bar{k}^2 - \bar{k}^2 = \int_t^{t+1} [k(s) - \bar{k}(t)]^2 ds \geq 0. \tag{B 10}$$

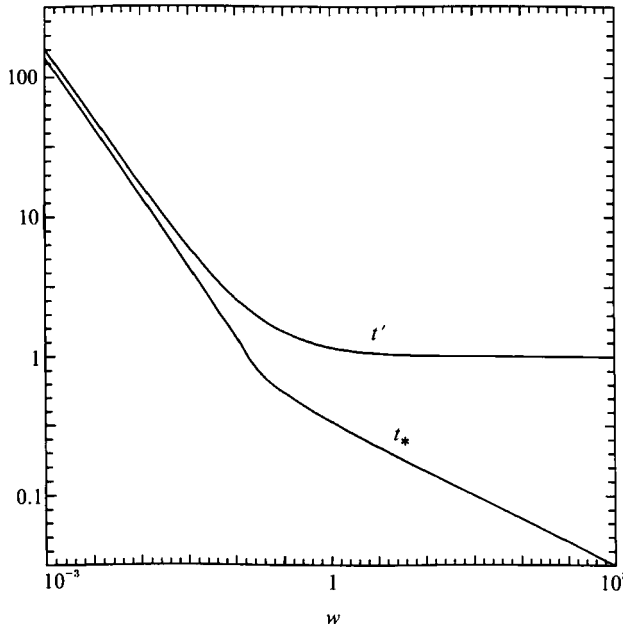


FIGURE 19. Time t_* to cusp formation and upper bound t' for propagating surface in pulsating flow.

To provide an initial condition, $\bar{k}(0)$, we integrate (B 7) twice to yield

$$\bar{k}(0) = 2\pi + w \int_0^1 \int_0^1 k(s)^2 ds dt \geq 2\pi. \tag{B 11}$$

It follows from (B 9) and (B 11) that $\bar{k}(t)$ is bounded below by $\tilde{k}(t)$, the solution to

$$d\tilde{k}/dt = w\tilde{k}^2 \tag{B 12}$$

with the initial condition $\tilde{k}(0) = 2\pi$:

$$\tilde{k} = 2\pi/(1 - 2\pi wt). \tag{B 13}$$

Clearly \tilde{k} becomes infinite at $\tilde{t} \equiv (2\pi w)^{-1}$, and this provides an upper bound on the time \bar{t} at which \bar{k} becomes infinite. And a singularity in \bar{k} at time \bar{t} implies a singularity in $k(t)$ by $\bar{t} + 1$. Thus, an upper bound on the time t_* to form a cusp is

$$t_* \leq t' \equiv 1 + 1/(2\pi w). \tag{B 14}$$

The time to cusp formation t_* , as a function of w , was determined by integrating (B 7) numerically. The result, together with the upper bound t' , is shown on figure 19. It may be seen that for small w , t' provides an accurate bound.

The travelling wave velocity field does not admit such a simple analysis, primarily because the location of cusp formation is not known *a priori*. However, using the infinitesimal element method, the time to singularity has been computed for several values of w . From the results (not shown) it appears that the time to cusp formation, again, varies as w^{-1} for small w .

In this Appendix, numerical tests have been performed to confirm the accuracy of the infinitesimal surface element method. In doing so, we address two statements made in Ashurst *et al.* (1988):

(i) 'pulsating flow damps the appearance of flame cusps so strongly that in the limit of infinite frequency we should expect to observe a flat laminar flame';

(ii) 'when $\omega > ku_L$ we do not observe this cusp shape but instead obtain a gentle sine wave response'.

A generalization of our result (B 14) (to pulsating flow of frequency ω , spatial period L , velocity u and flame speed w) is that an upper bound on the time to the cusp formation is

$$t^* = \omega^{-1} + \omega L^2 / (2\pi w u).$$

Thus we are in agreement on statement (i), since $\omega \rightarrow \infty$ implies $t^* \rightarrow \infty$. But for finite values of the parameters – however large $\omega L/w$ (i.e. $\omega/(ku_L)$) in the notation of Ashurst *et al.*) – t^* is finite. Hence we disagree with statement (ii) about the pulsating velocity field. It is also found that in a travelling wave velocity field, cusps form for the smallest speed considered ($w = 10^{-3}$). The numerical evidence suggests that for this case too, t^* varies as w^{-1} , but this is not proved.

REFERENCES

- ASHURST, W. T., SIVASHINSKY, G. I. & YAKHOT, V. 1988 Flame-front propagation in nonsteady hydrodynamic fields. *Combust. Sci. Tech.* **64**, 273.
- BATCHELOR, G. K. 1952 The effect of homogeneous turbulence on material lines and surfaces. *Proc. R. Soc. Lond. A* **213**, 349.
- BATCHELOR, G. K. 1959 Small-scale variation of convected quantities like temperature in turbulent fluid. Part 1. *J. Fluid Mech.* **5**, 113.
- CSANADY, G. T. 1970 *Turbulent Diffusion in the Environment*. Riedel.
- DO CARMO, M. P. 1976 *Differential Geometry of Curves and Surfaces*. Prentice-Hall.
- DRUMMOND, I. T. & MÜNCH, W. 1990 Turbulent stretching of material elements. *J. Fluid Mech.* **215**, 45.
- DRUMMOND, I. T. & MÜNCH, W. 1991 Distortion of line and surface elements in turbulent flows. *J. Fluid Mech.* **225**, 529.
- ESWARAN, V. & POPE, S. B. 1988 An examination of forcing in direct numerical simulations of turbulence. *Comput. Fluids* **16**, 257.
- GIRIMAJI, S. S. 1991 Asymptotic behavior of curvature of surface elements in turbulence. *Phys. Fluids A* **3**, 1772–1777.
- GIRIMAJI, S. S., POPE, S. B. 1990 Material element deformation in isotropic turbulence. *J. Fluid Mech.* **220**, 427.
- KRAICHNAN, R. H. 1974 Convection of a passive scalar by a quasi-uniform random straining field. *J. Fluid Mech.* **64**, 737.
- PETERS, N. 1988 Laminar flamelet concepts in turbulent combustion. In *Twenty-first Symp. (Intl) on Combustion*, pp. 1231–1250. Pittsburgh: The Combustion Institute.
- POPE, S. B. 1988 Evolution of surfaces in turbulence. *Intl. J. Engng Sci.* **26**, 445–469.
- POPE, S. B., YEUNG, P. K. & GIRIMAJI, S. S. 1989 The curvature of material surfaces in isotropic turbulence. *Phys. Fluids A* **1**, 2010–2018.
- ROGALLO, R. S. 1981 Numerical experiments in homogeneous turbulence. *NASA TM* 81315.
- YEUNG, P. K., GIRIMAJI, S. S. & POPE, S. B. 1990 Straining and scalar dissipation on material surfaces in turbulence: Implications for flamelets. *Combust. Flame* **79**, 340–365.
- YEUNG, P. K. & POPE, S. B. 1988 An algorithm for tracking fluid particles in numerical simulations of homogeneous turbulence. *J. Comput. Phys.* **79**, 373.
- YEUNG, P. K. & POPE, S. B. 1989 Lagrangian statistics from direct numerical simulations of isotropic turbulence. *J. Fluid Mech.* **207**, 531.